

Thermalization in massive deformations of Yang-Mills matrix models

ONUR OKTAY*

We numerically study the classical evolution of a Yang-Mills matrix model with two distinct mass deformation terms, which can be contemplated as a massive deformation of the bosonic part of the BFSS model. Through numerical analysis, it is shown that when the simulations are started from a certain set of initial conditions, thermalization occurs. Besides, an estimation method is proposed to determine the approximate thermalization time. Using this method, we demonstrate that thermalization time vary logarithmically with increasing matrix size when the mass terms differ. Introducing a matrix configuration, we also obtain reduced actions and subsequently analyze how the thermalization time change as a function of the energy.

1. Introduction

Since the introduction of the gauge/gravity duality [1, 2], there has been an immense effort from the theoretical physics community to use holographic methods in order to gain enhanced understanding about various physical phenomena. The duality between a thermal state in the boundary theory and a black hole in the bulk has formed the backbone of these studies and enabled the researchers to associate the process of thermalization in a unitary field theory with the formation of a black hole in the dual side. Explaining the dynamics of thermalization in isolated quantum systems, which is a central problem in many-body physics [3, 4], has also been studied within the context of AdS/CFT by focusing on certain string theory-inspired constructions such as the BFSS [5] and BMN [6] matrix models.

Over a decade ago, the remaining mysteries about the nature of black holes have led to several speculations related to their quantum mechanical structure, some of which could be tested in matrix model environments. To elaborate, motivated by the arguments of [7], Sekino and Susskind have conjectured that black holes are fast scramblers i.e. they scramble information at a rate proportional to the logarithm of the number of degrees of freedom

*E-mail: oktay24005@gmail.com

[8]. The thermalization processes observed in the BMN model have been numerically investigated and reported in a series of papers [9, 10, 11]. In particular, the results obtained in [9] are intriguing as they are broadly consistent with the fast scrambling conjecture. Berenstein et al. have shown that simulations of thermalization in the BMN model provide numerical evidence for fast thermalization, which may also be interpreted to implicate fast scrambling.

On the other hand, extensive thermodynamic simulations of the BFSS model, including detailed numerical studies of thermalization times, have been performed in references [12, 13]. Furthermore, the relation between quantum chaos and thermalization has been recently explored in [14]. Besides these developments, it is essential to note that due to large number of degrees of freedom interacting through a quartic Yang-Mills potential, it does not appear quite possible that general solutions of the BFSS/BMN models can be determined. Even the smallest Yang-Mills matrix model with two 2×2 matrices and with $SU(2)$ gauge symmetry has not been completely solved until this date [15]. Thus, in order to reach meaningful results, instead of considering the whole matrix theory it seems reasonable to concentrate on simplified structures with less degrees of freedom. A convenient way of achieving this is to place prior constraints on the system at hand by starting the simulations with specified sets of initial conditions. Although one would ideally prefer to choose initial conditions with the aim of setting up a configuration, which resembles the phenomenon of scattering gravitons at high energies, currently this not possible in the BFSS case due to the insufficient understanding of graviton states in this matrix model [10]. Nevertheless, as it will be discussed shortly, valuable information regarding the thermalization phenomenon can still be gathered from certain gauge invariant massive deformations of the BFSS model.

In this paper, our main interest is to analyze the dynamics of thermalization in a Yang-Mills matrix model with two distinct mass deformation terms, whose emerging chaotic motions have been investigated in [16]. This model has the same matrix content as the bosonic part of the BFSS matrix model, but also contains mass deformation terms that keep the gauge invariance intact. The paper is structured as follows. Section 2 starts out with a brief introduction of the model, which is followed by the description of the initial conditions that are used in the simulations. In section 3, we investigate the thermalization processes observed in the matrix model with massive deformations by performing a detailed numerical analysis of its classical evolution. This is followed by an examination of the variation of thermalization time with respect to matrix size. Then, by introducing a configuration of matrices, we obtain reduced actions from the full matrix model and subsequently explore the change of thermalization time with the

energies of these reduced actions. Lastly, section 4 is devoted to conclusions and outlook.

2. Yang-Mills matrix model with double mass deformation

The BFSS matrix model is a Yang-Mills theory in $0 + 1$ dimensions which arises from the dimensional reduction of the Yang-Mills theory in $9 + 1$ dimensions with $\mathcal{N} = 1$ supersymmetry [5]. In this paper, we focus upon a gauge invariant double mass deformation of the bosonic part of the BFSS action which may be specified as [16]

$$S = \frac{1}{g^2} \int dt \operatorname{tr} \left(\frac{1}{2} (D_t B_I)^2 + \frac{1}{4} [B_I, B_J]^2 - \frac{1}{2} \mu_1^2 B_i^2 - \frac{1}{2} \mu_2^2 B_k^2 \right), \quad (1)$$

where the indices i and k take on the values $i = 1, 2, 3$ and $k = 4, 5, 6$, respectively. In (1), B_I ($I = 1, \dots, 9$) are $N \times N$ Hermitian matrices and tr stands for the trace. The covariant derivatives are defined by

$$D_t B_I = \partial_t B_I - i[A, B_I]. \quad (2)$$

When the deformation parameters μ_1 and μ_2 are both equal to zero, (1) reduces to the bosonic part of the classical BFSS action. Since, we are going to be essentially concerned with the classical dynamics of (1), we absorb the coupling constant in the definition of \hbar , as it only determines the overall scale of energy classically.

In the Weyl gauge, $A = 0$, the equations of motion for B_I take the form

$$\ddot{B}_i + [B_I, [B_I, B_i]] + \mu_1^2 B_i = 0, \quad (3a)$$

$$\ddot{B}_k + [B_I, [B_I, B_k]] + \mu_2^2 B_k = 0, \quad (3b)$$

$$\ddot{B}_r + [B_I, [B_I, B_r]] = 0, \quad (3c)$$

where the index r runs through the values 7, 8, and 9. Similarly, the Weyl gauge Hamiltonian reads

$$H = \operatorname{tr} \left(\frac{P_I^2}{2} - \frac{1}{4} [B_I, B_J]^2 + \frac{1}{2} \mu_1^2 B_i^2 + \frac{1}{2} \mu_2^2 B_k^2 \right). \quad (4)$$

Due to gauge invariance, B_I matrices and conjugate momenta should also satisfy the Gauss Law constraint given by

$$[B_I, P_I] = 0. \quad (5)$$

The Hamilton's equations of motion can easily be derived from (4). However, in order to obtain relations that are more convenient for numerical

simulations, we rename a subset of phase space coordinates (namely B_I and P_I for $I \geq 4$) and subsequently change the indices labelling the aforementioned coordinates so that all indices can range over the same set of integer values. The resulting equations of motion can be written out as follows

$$\dot{P}_i = [[B_j, B_i], B_j] + [[C_l, B_i], C_l] + [[D_s, B_i], D_s] - \mu_1^2 B_i, \quad (6a)$$

$$\dot{R}_l = [[B_i, C_l], B_i] + [[C_{l'}, C_l], C_{l'}] + [[D_s, C_l], D_s] - \mu_2^2 C_l, \quad (6b)$$

$$\dot{W}_s = [[B_i, D_s], B_i] + [[C_l, D_s], C_l] + [[D_{s'}, D_s], D_{s'}], \quad (6c)$$

$$P_i = \dot{B}_i, \quad R_l = \dot{C}_l, \quad W_s = \dot{D}_s, \quad (6d)$$

where $j, l, l', s, s' = 1, 2, 3$. Furthermore, in this new notation (5) becomes

$$G = [B_i, P_i] + [C_l, R_l] + [D_s, W_s] = 0. \quad (7)$$

One of the primary purposes of this study is to examine the dependence of thermalization on the choice of initial conditions. To this end, we adopt an approach similar to the one suggested in [9] and set up the initial conditions as follows

$$B_1 = \begin{pmatrix} J_1 & 0 \\ 0 & 0 \end{pmatrix}, \quad B_2 = \begin{pmatrix} J_2 & q_1 \\ q_1^\dagger & 0 \end{pmatrix}, \quad B_3 = \begin{pmatrix} J_3 & q_2 \\ q_2^\dagger & 0 \end{pmatrix}, \quad C_l = \begin{pmatrix} J_l & 0 \\ 0 & 0 \end{pmatrix}$$

$$P_1 = \begin{pmatrix} 0 & 0 \\ 0 & p_0 \end{pmatrix}, \quad P_2 = P_3 = 0, \quad D_s = 0, \quad R_l = W_s = 0, \quad (8)$$

where J_i 's are $(N - 1)$ -dimensional Hermitian matrices. They denote the spin- j ($j = (N - 2)/2$) irreducible representation of $SU(2)$ and form the fuzzy two-sphere at level j [19, 20]. While the diagonal modes of B_i and C_l matrices start from the fuzzy sphere configurations, P_1 initiates with a single eigenvalue, p_0 , on the main diagonal. Besides their diagonal modes, the off-diagonal elements of B_2 and B_3 are also excited with the addition of q_1 and q_2 blocks that are consisting of randomly generated initial conditions. These blocks, which serve as sources of small fluctuations, are formed by utilizing a complex normal distribution with a spread proportional to $(\hbar/(N - 1))^{\frac{1}{2}}$. After completing the essential procedure of specifying initial conditions, we may now proceed to the stage of numerical simulations.

3. Numerical results

This section is devoted to an investigation of the thermalization processes observed in the Yang-Mills theory with massive deformations. In order to provide a comprehensive analysis, we carry out numerical simulations for the time evolution of (6). After discretizing the equations of motion, an iterative

algorithm can be developed to solve the discretized equations numerically. By saving the contents of the eighteen matrices every few iterations, one can gain valuable insight into the dynamics of thermalization as will be discussed shortly.

In the computations, a simulation code implemented in Matlab is used. The code is executed with a constant time step of 0.004 and we run it for a sufficient amount of time to clearly observe the values that the eigenvalues converge to. Due to truncation of digits, errors are inevitable in numerical calculations. In this regard, although the initial conditions given by (8) fulfill the Gauss law constraint, the cumulative effect of rounding errors could cause the violation of (7). However, by constantly monitoring G during the the trial runs of the simulation, we made sure that no such effect is present.

Having now introduced the basic features of numerical computations, we move on to the details of obtained results. When the random fluctuation terms are not added to the system, i.e. $\hbar = 0$, the starting configurations keep evolving periodically in time and thermalization does not occur. Thus, to avoid such a scenario, we set the value of \hbar to 0.001, which will remain fixed for the rest of this work. In order to discover various intriguing properties of the thermalization process, we first vary the p_0 parameter. Figure 1 shows the evolution of the eigenvalues of B_1 with simulation time for six different p_0 values. The first thing we can immediately observe from the plots

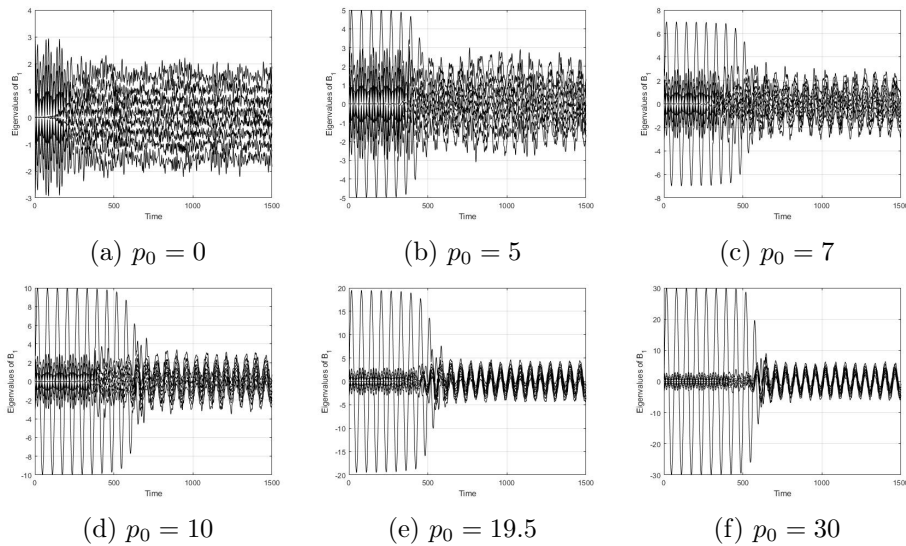


Fig. 1: Eigenvalues of B_1 vs. Time at $N = 8$, $\mu_1 = 1$, and $\mu_2 = 1.5$

is that the oscillatory behavior of eigenvalues, which can be most clearly seen from the last two figures, become more apparent with increasing p_0 . In

Figures 1e and 1f, after a series of oscillations, the amplitudes of the oscillations decrease considerably and the frequencies tend to synchronize which results in the emergence of collective oscillations.

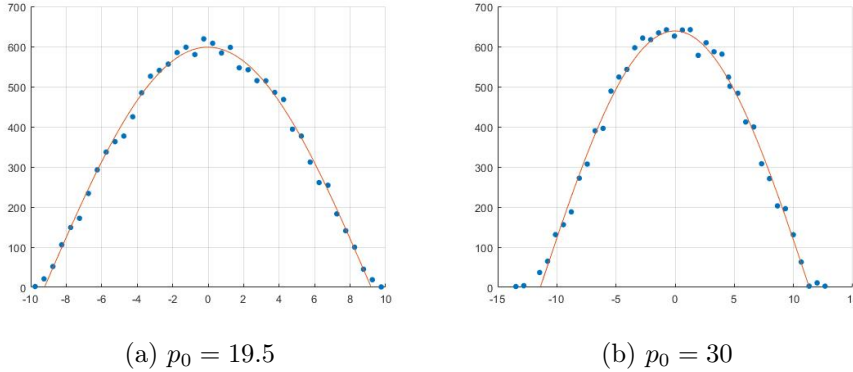


Fig. 2: Histograms of eigenvalues of P_1 at $N = 8$, $\mu_1 = 1$, and $\mu_2 = 1.5$

On the other hand, as it is described in detail in subsection 3.1, thermalization occurs at all six p_0 values that are used in preparation of Figure 1. In order to probe the presence of thermalization occurring at the p_0 values of 19.5 and 30, let us consider the results shown on Figure 2. In Figures 2a and 2b, the eigenvalue distributions of the momentum matrix P_1 are illustrated. The histograms are generated by sampling the eigenvalues of P_1 on the time interval[†] [758, 2500] during which the system resides in potentially thermalized states. The bin size is set to 40 and the dots in the figure correspond to the midpoints of the top edges of histogram bars. As expected from thermalized configurations, the semicircle distribution model fits the data nicely in both cases. Furthermore, in order to compare the eigenvalue distributions of the momenta matrices, the histograms of the eigenvalues of P_1 and R_1 are plotted together in Figure 3. This time the histograms are generated by sampling the eigenvalues on the time interval [758, 3000] with a bin size equal to 30. Let us also note that we now set the value of p_0 to 30, which will remain fixed for the rest of this work unless otherwise stated. It appears that the semicircle model gives an essentially good fit to both P_1 and R_1 distributions, which implies that after $t = 758$ momenta temperatures become essentially the same. Thus, it is safe to conclude that thermalization has occurred.

[†]A detailed discussion of the determination of thermalization times is given in the next subsection.

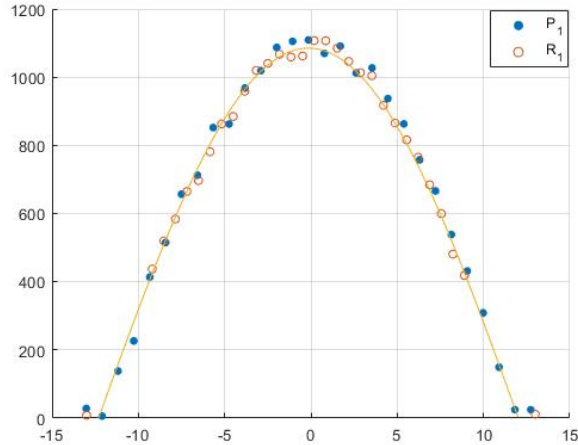


Fig. 3: Histograms of eigenvalues of P_1 and R_1 at $N = 8$, $\mu_1 = 1$, and $\mu_2 = 1.5$

3.1. Thermalization time

The main results concerning the presence of thermalization have been discussed up to this point. As it is central to the understanding of the thermalization process, let us consider a method that will help us in both determining the thermalization time of the system and providing evidence for the presence of thermalization. This method relies on the evaluation of the relative size of changes in both B_i and C_i eigenvalues [9].

Figure 4 displays how the standard deviations of the eigenvalues for B_1 , B_2 , C_1 , and C_2 matrices evolve with simulation time. As seen in the legend, $\text{std}(B_1)$ denotes the standard deviation of the eigenvalues for B_1 and so on. Starting from oscillatory behavior with nearly constant amplitude, $\text{std}(B_1)$ undergoes a change at $t \gtrsim 500$ and its amplitude decrease considerably with time. In addition, as time progresses, the standard deviations tend to converge on a narrow band of values and the system reaches a seemingly stable configuration in which only minor fluctuations are observed.

Among the different notions of thermalization time, we choose to focus on the one that define it as the timescale of thermalization from a given set of initial conditions. Using the signal processing toolbox of Matlab, we have developed a code that detects the time instants at which the variance of a signal changes significantly and run it on the standard deviation data graphed in Figure 4. The approximate time when the standard deviations, hence the system, reaches an equilibrium size is determined to be equal to 758. In Figure 4, this approximate time instant is marked with a dashed

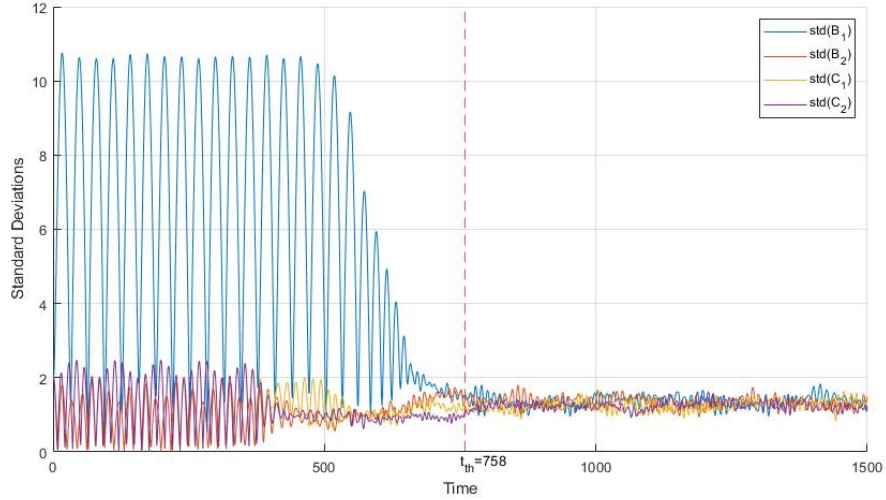


Fig. 4: Standard deviations of eigenvalues vs. Time at $N = 8$, $\mu_1 = 1$, and $\mu_2 = 1.5$

vertical line and t_{th} denotes the thermalization time of the system.

The procedure detailed above can be generalized for $N > 8$. In Figure 5, we present plots of thermalization time versus N at four distinct mass combinations, where the matrix size N takes the values $N = 8, \dots, 100$. Let us immediately note that the models at $\mu_1 = \mu_2 = 1$ have different features from the rest in the sense that data values tend to decrease with increasing N . We find that the function

$$T_1(N) = \frac{3404}{\sqrt{N}}, \quad (9)$$

provides an adequate fit to the data as can be seen from Figure 5a. In addition, a logarithmic fit of the form

$$T_a(N) = c_a \log(N) + d_a, \quad (10)$$

with

	c_a	d_a
$T_2(N)$	439.5	-284.9
$T_3(N)$	380.1	49.04
$T_4(N)$	419.4	-60.1

Table 1: c_a and d_a values for the fitting curve (10)

appears to be well-suited for the remaining models as can be observed from Figures 5b - 5d. In equation (10), the index a ranges from 2 to 4. Besides, it is important to note that expressions (9) and (10) are quite sufficient to fit the data as the minimum recorded adjusted R-squared value is equal to 0.938.

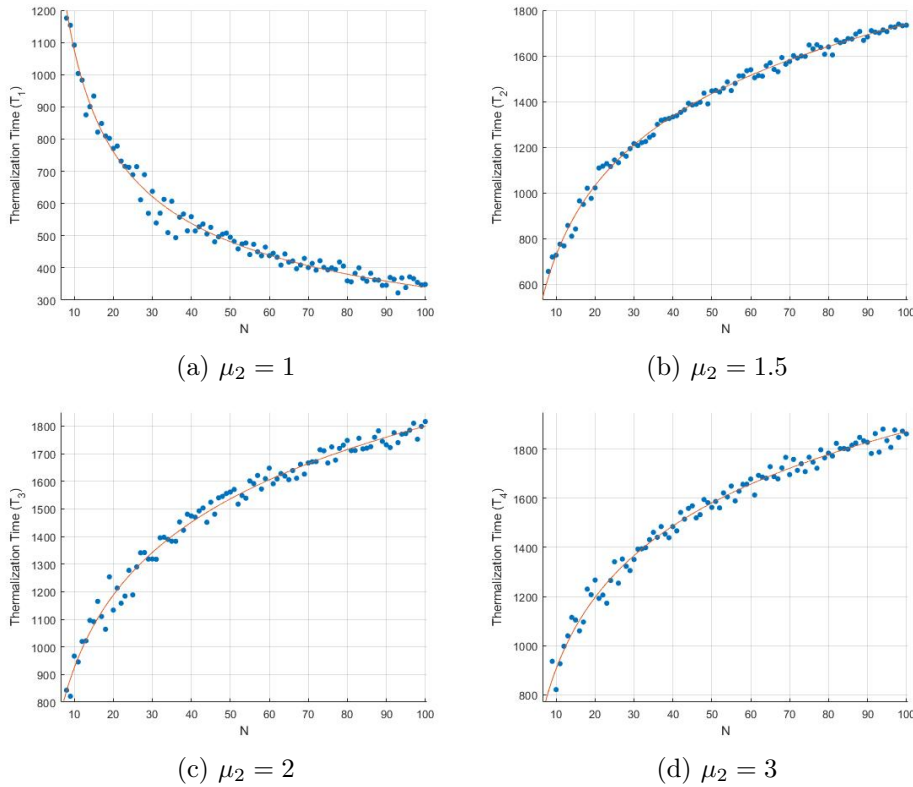


Fig. 5: Thermalization time vs. N at $\mu_1 = 1$

At a slight tangent to the analysis of thermalization times, let us return back to the study of Figure 4. The method used in the preparation of this figure can be applied with some arbitrary p_0 value of our choosing to produce a similar graph. In Appendix A, we display Figure 9, which shows the variations of the standard deviations of the eigenvalues for B_1 , B_2 , C_1 , and C_2 matrices at the p_0 values that are already utilized in the preparation of Figure 1. Similar to the behavior observed when p_0 is equal to 30, in Figures 9a-9e, after periods of decrease in oscillation amplitudes, standard deviations converge on narrow bands, which implies that thermalization occurs at all six p_0 values. To test this hypothesis, we may pick $p_0 = 7$ and

examine the eigenvalue distributions of the momenta matrices. In Figure 8, the histograms of the eigenvalues of P_1 and R_1 at $p_0 = 7$ are depicted together for the sake of comparison. Since the semicircle curve provides a good fit to both distributions, we can infer that the momenta temperatures are essentially the same and thermalization has occurred.

3.1.1. Energy dependence of thermalization time

Apart from its dependence to matrix size, we can also explore the variation of the thermalization time with respect to energy. In this subsection, by performing simulations of the matrix model (4), the dependence of thermalization time to energy is depicted at several distinct mass combinations and matrix size values.

We launch the discussion with introducing a matrix configuration in the form

$$\begin{aligned} B_1 &= \begin{pmatrix} v(t)J_1 & 0 \\ 0 & 0 \end{pmatrix}, & B_2 &= \begin{pmatrix} v(t)J_2 & q_1 \\ q_1^\dagger & 0 \end{pmatrix}, & B_3 &= \begin{pmatrix} v(t)J_3 & q_2 \\ q_2^\dagger & 0 \end{pmatrix}, \\ C_l &= \begin{pmatrix} z(t)J_l & 0 \\ 0 & 0 \end{pmatrix}, & P_1 &= \begin{pmatrix} 0 & 0 \\ 0 & p_0 \end{pmatrix}, & P_2 &= P_3 = 0, & R_l &= 0, \\ D_s &= 0, & W_s &= 0, \end{aligned} \tag{11}$$

where $v(t)$ and $z(t)$ are real functions of time and J_i satisfy the commutation relations given by $[J_i, J_j] = i\hbar_j \epsilon_{ijl} J_l$. After substituting configuration (11), at an arbitrary time t , into the Hamiltonian (4), we evaluate the traces using Matlab and arrive at a set of effective Hamiltonians[‡]. A generic member of this set can be expressed as follows

$$\begin{aligned} H_s &= \frac{1}{2}p_0^2 + \hbar_j^4 c_N (v^2 + z^2)^2 + \hbar_j^2 \left[(c_N \mu_1^2 + \Delta_1) v^2 + (c_N \mu_2^2 + \Delta_2) z^2 \right] \\ &\quad + \Delta_3 \mu_1^2, \end{aligned} \tag{12}$$

where the coefficients c_N are defined by $c_N = \frac{N(N-1)(N-2)}{8}$.

Here, it is essential to note that, due to the presence of fluctuation blocks q_1 and q_2 , unlike c_N , Δ_i coefficients are random numbers that change with every new substitution of the configuration (11) into (4). With the purpose of listing and examining Δ_i values, we have repeated the procedure utilized in the obtainment of H_s by running a code 500 times and determined the reduced Hamiltonians. For $N = 8$, the maximums of the absolute values of Δ_1 , Δ_2 , and Δ_3 were recorded as 0.0018, 0.0014, 0.0003 respectively, which

[‡]It is important to remark that we employ this method only for producing initial configurations. Unlike the reduced models in matrix model settings studied in [16, 17, 18], the matrix configuration defined by (11) does not satisfy the equations of motion (6).

indicates that the extent of change in the coefficients of quadratic terms is small (in comparison to c_N) but not negligible. Let us also add that we set \hbar_j to 1 in this subsection.

Another point to emphasize is that analyzing the classical dynamics of equation (12) is not a purpose of this study. H_s would be solely employed to generate initial conditions for the simulations of equation (4). In order to give a detailed description of the initial condition selection process, let us first denote by $(v_b, z_b) \equiv (v(t_b), z(t_b))$ a generic set of initial conditions at the start time t_b of a classical simulation of H . Then, at $t = t_b$, (12) can be expressed as shown below

$$E = c_N v_b^4 + c_N z_b^4 + (c_N \mu_1^2 + \Delta_1) v_b^2 + (c_N \mu_2^2 + \Delta_2) z_b^2 + 2c_N v_b^2 z_b^2 + \frac{1}{2} p_0^2 + \Delta_3 \mu_1^2, \quad (13)$$

where E is the energy of the reduced action.

With the aim of investigating the variance of thermalization time with energy, we run another Matlab code, which determines the thermalization time at several different values of the energy. We run the code with randomly selected initial conditions satisfying a given energy condition and detect the thermalization time of the system for a specified matrix size and mass combination. In order to give certain effectiveness to the random initial condition selection process, we developed a simple approach which we briefly explain next. To start with, we generate two uniformly distributed random numbers ϕ_ν over the interval $0 \leq \phi_\nu \leq E$ satisfying the constraint $E = \phi_1 + \phi_2$. Subsequently, the real roots of the expression

$$c_N z_b^4 + (c_N \mu_2^2 + \Delta_2) z_b^2 + \frac{1}{2} p_0^2 + \Delta_3 \mu_1^2 - \phi_1 = 0, \quad (14)$$

are found. Our code randomly selects one of these roots, which is later used to solve for v_b in the equation

$$c_N v_b^4 + (c_N \mu_1^2 + 2c_N z_b^2 + \Delta_1) v_b^2 - \phi_2 = 0. \quad (15)$$

Lastly, as the final step of the selection process, one of the real roots of equation (15) is randomly picked by our code. Having now determined the (v_b, z_b) pair, we move on to discuss the simulation stage. In order to measure the thermalization time at the energy E , we perform a classical simulation of the matrix model (4). This simulation is started with the

initial configuration given by

$$\begin{aligned}
 B_1 &= \begin{pmatrix} v_b J_1 & 0 \\ 0 & 0 \end{pmatrix}, & B_2 &= \begin{pmatrix} v_b J_2 & q_1 \\ q_1^\dagger & 0 \end{pmatrix}, & B_3 &= \begin{pmatrix} v_b J_3 & q_2 \\ q_2^\dagger & 0 \end{pmatrix}, \\
 C_l &= \begin{pmatrix} z_b J_l & 0 \\ 0 & 0 \end{pmatrix}, & P_1 &= \begin{pmatrix} 0 & 0 \\ 0 & p_0 \end{pmatrix}, & P_2 &= P_3 = 0, & R_l &= 0, \\
 D_s &= 0, & W_s &= 0.
 \end{aligned} \tag{16}$$

Following the completion of the classical simulation, the thermalization time is measured by the method described at the beginning of subsection 3.1. By setting p_0 equal to 12 and repeating the procedure detailed above for a range of energy values, the data used in the depiction of Figures 6 and 7 are prepared.

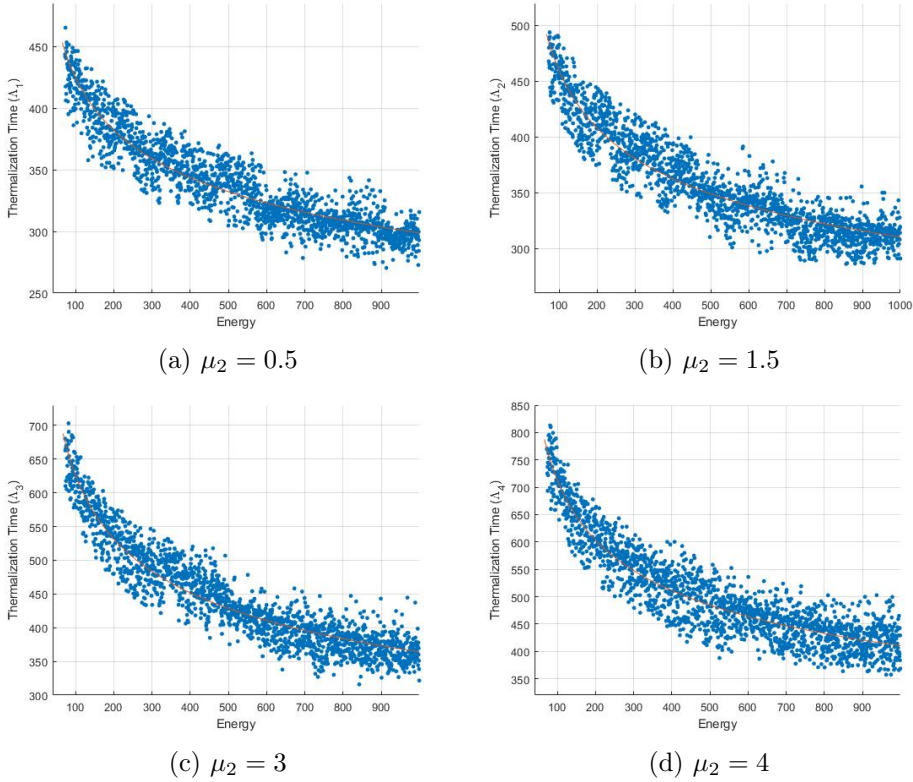


Fig. 6: Thermalization time vs. Energy at $\mu_1 = 1$ and $N = 8$

Figure 6 shows the plots of thermalization time versus energy at four different μ_2 values. The best-fitting function for the numerical data displayed

in Figure 6 is found to be a power law in the form

$$\Lambda_m(E) = \alpha_m E^{\beta_m} + \xi_m. \quad (17)$$

The fitting parameters of the best fit equations (17) are listed in Table 2. Due to the obvious increase in the variance of the data, the fits describing the thermalization times of

	α_m	β_m	ξ_m
$\Lambda_1(E)$	859.8	-0.1491	-8.2
$\Lambda_2(E)$	1007	-0.1737	6.9
$\Lambda_3(E)$	1850	-0.2353	0.4
$\Lambda_4(E)$	2153	-0.240	3.1

Table 2: α_m , β_m and ξ_m values for the fitting curve (17)

Figure 6 are not as good in comparison to the fits displayed in Figure 5. The four fitting curves Λ_m ($m = 1, 2, 3, 4$) appear to have the adjusted R-squared statistics of 0.8681, 0.8654, 0.897, and 0.8703 respectively.

On the other hand, in order to take the effects of matrix size into consideration, we illustrate in Figure 7 the evolutions of thermalization times with energy at $N = 6, 8, 10, 12$. From the profile of thermalization times with respect to energy shown in Figure 7, we observe that numerical data exhibits a decreasing trend, which can be modelled again with a power law in the form

$$\Gamma_m(E) = \theta_m E^{\epsilon_m} + \delta_m, \quad (18)$$

with the fitting parameters displayed in Table 3. The adjusted R-squared values of the

	θ_m	ϵ_m	δ_m
$\Gamma_1(E)$	1237	-0.1942	-3.4
$\Gamma_2(E)$	1007	-0.1737	6.9
$\Gamma_3(E)$	1291	-0.1825	33.7
$\Gamma_4(E)$	1128	-0.1796	1.8

Table 3: θ_m , ϵ_m and δ_m values for the fitting curve (18)

fitting curves depicted in Figures 7a - 7d are given by 0.8548, 0.8654, 0.8722 and 0.855 respectively, which essentially indicates that Γ_m curves provide adequate fits to the numerical data.

4. Conclusions and outlook

In this paper, we have considered the dynamics of thermalization in a Yang-Mills matrix model with two distinct mass deformation terms, which

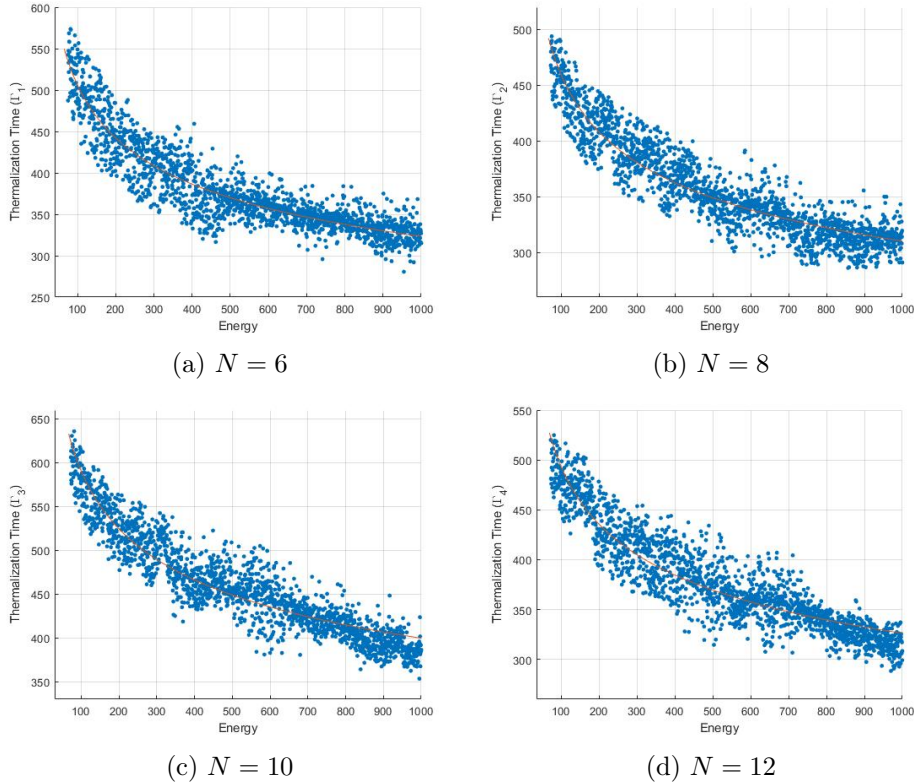


Fig. 7: Thermalization time vs. Energy at $\mu_1 = 1$ and $\mu_2 = 1.5$

may be contemplated as a double mass deformation of the bosonic part of the BFSS model. We have performed a detailed numerical analysis of the classical evolution of this model and determined that when the simulations are started from a certain set of initial conditions, thermalization occurs. Although small background fluctuations are required to initiate thermalization, from the findings of numerical simulations it was clearly seen that thermalization times are independent of these fluctuations. This is an extension of the result given in [12] for the BFSS model.

From the results concerning the change in thermalization times with respect to matrix size, we were able to demonstrate through an appropriate fitting function that thermalization times vary logarithmically with matrix size when the mass parameters μ_1 and μ_2 differ. It is worth mentioning that in reference [8], thermalization (or scrambling) time of a black hole is conjectured to be proportional to $\log(N)$ where N is the number of degrees of freedom. Even though we have adopted a different definition of thermaliza-

tion time, it is still interesting to note that the findings obtained for Hamiltonian (4) confirm this conjecture. In subsection 3.1, we have also presented plots depicting the variations of thermalization times with respect to the energies of the reduced actions and subsequently the best-fitting functions for the data were determined as power laws. A common feature observed in all fitting functions is that thermalization times converge to finite values in the large energy or matrix size limit.

Let us also mention some recent developments in related subjects. Although calculating entanglement entropy in ordinary field theories is a rather difficult task, calculations in noncommutative theories such as the scalar field theory on the fuzzy sphere were already carried out in [21, 22, 23]. Moreover, numerical computations of entanglement entropy in the BFSS matrix model were recently performed in [14]. Besides, the behavior of entanglement entropy during thermalization was studied in holographic systems in references [24, 25, 26]. Based on these considerations, a valuable direction of research would be to investigate the time dependence of entanglement entropy in the system defined by (4). Particularly, it would be interesting to explore the possible use of entanglement entropy as a probe of thermalization. Another challenging direction of development is to analyze the dynamics of quantum chaos with emphasis on the measurements of Lyapunov exponents and check whether our model saturates the Maldacena-Shenker-Stanford bound [27] or not. We hope that these issues will produce useful results to be reported soon.

REFERENCES

- [1] J. M. Maldacena, «The Large N limit of superconformal field theories and supergravity», *Int. J. Theor. Phys.* **38**, 1113 (1999).
- [2] E. Witten, «Anti-de Sitter space and holography», *Adv. Theor. Math. Phys.* **2**, 253 (1998).
- [3] M. Srednicki, «Chaos and quantum thermalization», *Phys. Rev. E* **50**, 888 (1994).
- [4] J.M. Deutsch, «Quantum statistical mechanics in a closed system», *Phys. Rev. A* **43**, 2046 (1991).
- [5] T. Banks, W. Fischler, S. H. Shenker and L. Susskind, «M theory as a matrix model: A Conjecture», *Phys. Rev. D* **55**, 5112 (1997).
- [6] D. E. Berenstein, J. M. Maldacena and H. S. Nastase, «Strings in flat space and pp waves from N=4 superYang-Mills», *JHEP* **04**, 013 (2002).
- [7] P. Hayden and J. Preskill, «Black holes as mirrors: Quantum information in random subsystems», *JHEP* **09**, 120 (2007).
- [8] Y. Sekino and L. Susskind, «Fast Scramblers», *JHEP* **10**, 065 (2008).

- [9] C. Asplund, D. Berenstein and D. Trancanelli, «Evidence for fast thermalization in the plane-wave matrix model», *Phys. Rev. Lett.* **107**, 171602 (2011).
- [10] D. Berenstein and D. Trancanelli, «Dynamical tachyons on fuzzy spheres», *Phys. Rev. D* **83**, 106001 (2011).
- [11] C. T. Asplund, D. Berenstein and E. Dzienkowski, «Large N classical dynamics of holographic matrix models», *Phys. Rev. D* **87**, 084044 (2013).
- [12] P. Riggins and V. Sahakian, «On black hole thermalization, D0 brane dynamics, and emergent spacetime», *Phys. Rev. D* **86**, 046005 (2012).
- [13] S. Aoki, M. Hanada and N. Iizuka, «Quantum Black Hole Formation in the BFSS Matrix Model», *JHEP* **07**, 029 (2015).
- [14] P. V. Buividovich, M. Hanada and A. Schäfer, «Quantum chaos, thermalization, and entanglement generation in real-time simulations of the Banks-Fischler-Shenker-Susskind matrix model», *Phys. Rev. D* **99**, 046011 (2019).
- [15] D. Berenstein and D. Kawai, «Smallest matrix black hole model in the classical limit», *Phys. Rev. D* **95**, 106004 (2017).
- [16] K. Başkan, S. Kürkçüoğlu, O. Oktay and C. Taşcı, «Chaos from Massive Deformations of Yang-Mills Matrix Models», *JHEP* **10**, 003 (2020).
- [17] I. Y. Aref'eva, P. B. Medvedev, O. A. Rytchkov and I. V. Volovich, «Chaos in M(atric) theory», *Chaos Solitons Fractals* **10**, 213 (1999).
- [18] Y. Asano, D. Kawai and K. Yoshida, «Chaos in the BMN matrix model», *JHEP* **06**, 191 (2015).
- [19] J. Madore, «The Fuzzy sphere», *Class. Quant. Grav.* **9**, 69 (1992).
- [20] A. P. Balachandran, S. Kurkcuoğlu and S. Vaidya, «*Lectures on fuzzy and fuzzy SUSY physics*», (World Scientific, 2007).
- [21] D. Dou and B. Ydri, «Entanglement entropy on fuzzy spaces», *Phys. Rev. D* **74**, 044014 (2006).
- [22] J. L. Karczmarek and P. Sabella-Garnier, «Entanglement entropy on the fuzzy sphere», *JHEP* **03**, 129 (2014).
- [23] S. Okuno, M. Suzuki and A. Tsuchiya, «Entanglement entropy in scalar field theory on the fuzzy sphere», *PTEP* **2016**, 023B03 (2016).
- [24] H. Liu and S. J. Suh, «Entanglement growth during thermalization in holographic systems», *Phys. Rev. D* **89**, 066012 (2014).
- [25] I. Y. Aref'eva, M. A. Khramtsov and M. D. Tikhonovskaya, «Thermalization after holographic bilocal quench», *JHEP* **09**, 115 (2017).
- [26] I. Y. Aref'eva, A. Patrushev and P. Slepov, «Holographic entanglement entropy in anisotropic background with confinement-deconfinement phase transition», *JHEP* **07**, 043 (2020).
- [27] J. Maldacena, S. H. Shenker and D. Stanford, «A bound on chaos», *JHEP* **08**, 106 (2016).

Appendix A

Additional figures

In this appendix, we present Figures 8 and 9. We illustrate in Figure 8 the eigenvalue distributions of P_1 and R_1 at $p_0 = 7$. The histograms are generated by sampling the momenta eigenvalues on the time interval $[827, 3000]$ with a bin size equal to 40. In Figure 9, the time evolutions of the standard deviations of the eigenvalues for $B_1, B_2, C_1,$ and C_2 matrices at six different p_0 values are displayed.

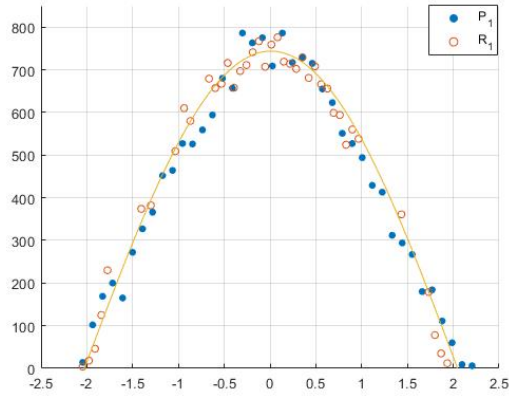
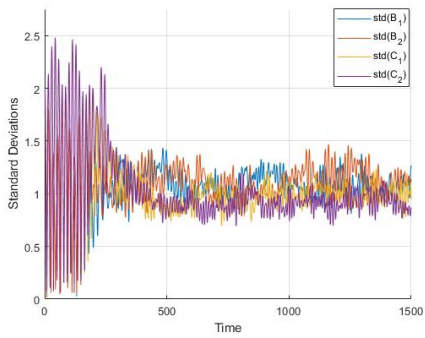
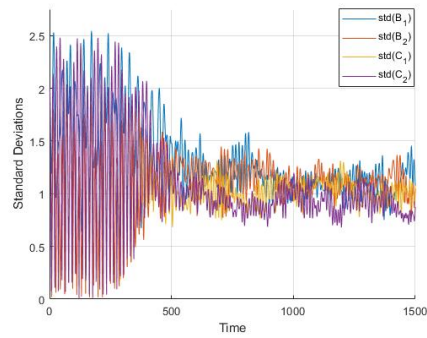


Fig. 8: Histograms of eigenvalues of P_1 and R_1 at $N = 8, p_0 = 7, \mu_1 = 1,$ and $\mu_2 = 1.5$



(a) $p_0 = 0$



(b) $p_0 = 5$

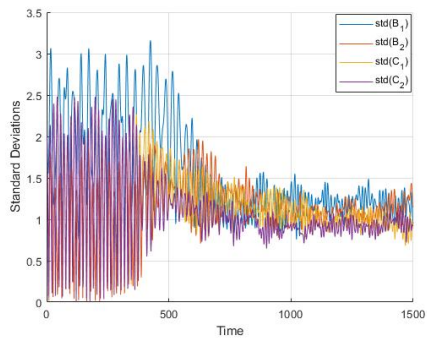
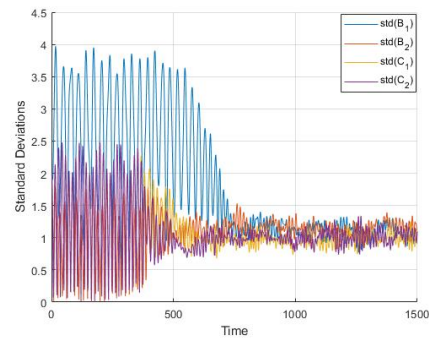
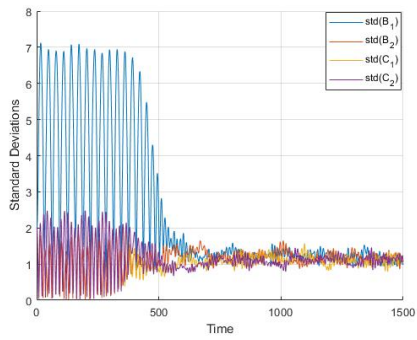
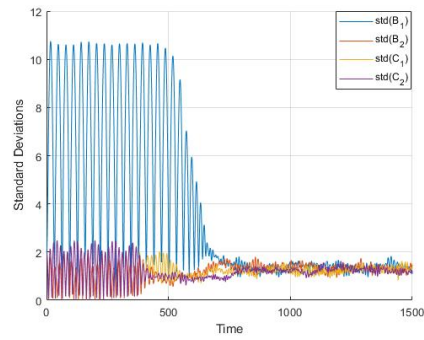
(c) $p_0 = 7$ (d) $p_0 = 10$ (e) $p_0 = 19.5$ (f) $p_0 = 30$

Fig. 9: Standard deviations of eigenvalues vs. Time at $N = 8$, $\mu_1 = 1$, and $\mu_2 = 1.5$